Theoretical and Applied Fracture Mechanics 107 (2020) 102510

Contents lists available at ScienceDirect

Theoretical and Applied Fracture Mechanics

journal homepage: www.elsevier.com/locate/tafmec

Low cycle fatigue life modelling using finite element strain range partitioning for a steam turbine rotor steel

Ahmed Azeez[a,*], Robert Eriksson[a], Daniel Leidermark[a], Mattias Calmunger[b]

[a] Division of Solid Mechanics, Linköping University, 58183 Linköping, Sweden
[b] Division of Engineering Materials, Linköping University, 58183 Linköping, Sweden

ARTICLE INFO

Keywords:
Creep-fatigue interaction
Creep-resistant steel
EBSD
Low cycle fatigue
Steam turbine steel
Strain range partitioning

ABSTRACT

Materials made for modern steam power plants are required to withstand high temperatures and flexible operational schedule. Mainly to achieve high efficiency and longer components life. Nevertheless, materials under such conditions experience crack initiations and propagations. Thus, life prediction must be made using accurate fatigue models to allow flexible operation. In this study, fully reversed isothermal low cycle fatigue tests were performed on a turbine rotor steel called FB2. The tests were done under strain control with different total strain ranges and temperatures (20 °C to 625 °C). Some tests included dwell time to calibrate the short-time creep behaviour of the material. Different fatigue life models were evaluated based on total life approach. The stress-based fatigue life model was found unusable at 600 °C, while the strain-based models in terms of total strain or inelastic strain amplitudes displayed inconsistent behaviour at 500 °C. To construct better life prediction, the inelastic strain amplitudes were separated into plastic and creep components by modelling the deformation behaviour of the material, including creep. Based on strain range partitioning approach, the fatigue life depends on different damage mechanisms at different strain ranges at 500 °C. This allows for the formulation of life curves based on either plasticity-dominated damage or creep-dominated damage. At 600 °C, creep dominated while at 500 °C creep only dominates for higher strain ranges. The deformation mechanisms at different temperatures and total strain ranges were characterised by scanning electron microscopy and by quantifying the amount of low angle grain boundaries. The quantification of low angle grain boundaries was done by electron backscatter diffraction. Microscopy revealed that specimens subjected to 600 °C showed signs of creep damage in the form of voids close to the fracture surface. In addition, the amount of low angle grain boundaries seems to decrease with the increase in temperature even though the inelastic strain amplitude was increased. The study indicates that a significant amount of the inelastic strain comes from creep strain as opposed of being all plastic strain, which need to be taken into consideration when constructing a life prediction model.

1. Introduction

Increase of thermal efficiency in steam turbines is desired, but restrictions from the material properties limit this advancement. The components subjected to the highest temperatures and pressure in the steam turbine are usually made of materials that can withstand fatigue and creep. The development of the 9–12% Cr steel class with high resistance to creep allows for the possibility to produce steam power plants with Ultra-Supercritical steam conditions, i.e. temperature and pressure of 600–620 °C and 300 bar, respectively [1,2].

Turbine components are subjected to cyclic loading mainly due to the operation schedule. To improve fatigue life predictions and provide better maintenance intervals, accurate fatigue life models at high temperatures are required. Yimin and Jinrui [3] investigated the low cycle fatigue (LCF) behaviour of 30Cr2MoV rotor steel at high temperatures and stressed the importance of designing rotors based on cyclic conditions while taking the creep properties of the material into account. High-temperature fatigue analyses on the 9–12% Cr steel class were done by Mishnev et al. [4] and Guguloth et al. [5], showing that martensitic steels experience a cyclic softening behaviour at all temperatures. Fatigue life models based on the Manson–Coffin and Basquin relations [6], were also studied in these papers. Cyclic loading of materials above the yield limit produces plastic straining, but at high temperatures creep contribution becomes significant and has to be taken into account. A creep–fatigue interaction analysis is usually used to quantify the respective contributions of creep and fatigue damage [7–9]. The strain range partitioning (SRP) approach is one method for separating the inelastic strain range into plastic and creep components

* Corresponding author.
E-mail address: ahmed.azeez@liu.se (A. Azeez).

https://doi.org/10.1016/j.tafmec.2020.102510

Available online 05 February 2020

Table 1
The nominal composition of FB2 in wt.% [1].

Material	C	Mn	N	Al	Co	Cr	Mo	Nb	Ni	V	B	Fe
FB2	0.12	0.9	0.02	<0.01	1.0	9	1.5	0.06	0.2	0.21	0.011	bal.

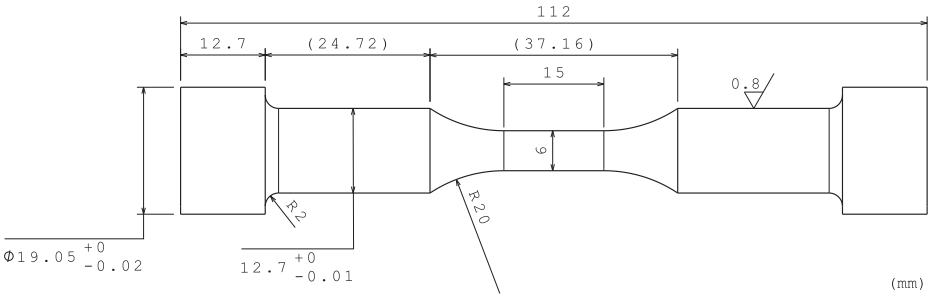

Fig. 1. Smooth button head cylindrical specimen used in the LCF testing.

Table 2
Isothermal LCF tests done on the rotor steel FB2.

Temperature, °C	$\Delta\varepsilon_t$, %	Dwell time, min	No. tests	N_f, Cycles	t_f, h
20	0.6	–	1	8910	29.70
20	0.8	–	1	4224	18.77
20	1.2	–	1	1820	12.13
400	0.8	–	1	2735	12.15
400	1.2	–	1	1349	8.99
500	0.8	–	2	2714; 3111	12.06; 13.82
500	1.2	–	1	807	5.38
600	0.8	–	2	1344; 1360	5.97; 6.04
600	1.2	–	1	789	5.26
500	0.8	5	1	1860	318.26
550	0.8	5	1	1580	270.35
600	0.8	5	1	870	148.86
625	0.8	5	1	730	124.91

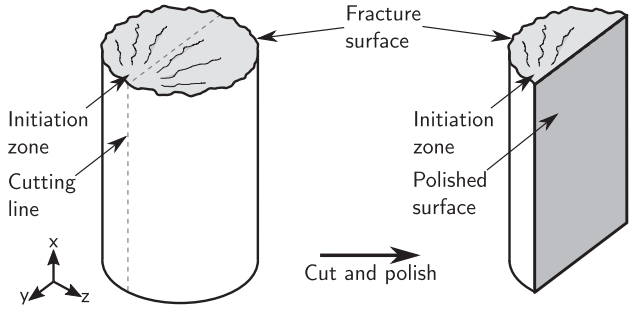

Fig. 2. Illustration of the sample preparation process done prior to the microstructure investigation on the polished surface.

[10], which can subsequently be used to evaluate the fatigue life. It was shown by Mishnev et al. [11] that lower strain rates produce larger inelasticity at high temperature for creep-resistant martensitic steels. This could be attributed to creep, as the material spends longer time at high stresses. Thus, partitioning of the inelastic strain helps to characterise the material behaviour and predicts the fatigue life more accurately.

In this study, the deformation behaviour of the rotor steel FB2 was evaluated using finite element (FE) simulations under given conditions. The parameters of the used contitutive and fatigue life models were fitted from mid-life LCF tests presented in this study. The analysis aims to separate the creep strain from plastic strain in the FE analysis which helps to better explain the fatigue behaviour. The study also investigates the mechanisms behind the effect of temperature on fatigue life by carrying out a microstructural analysis to inspect the contribution of inelasticity and the effect of temperature on life under LCF loading.

2. Material and testing

The rotor steel investigated in this research is 9CrMoCoVNbNB, or X13-CrMoCoVNbNB9-2–1 (German designation), which is commonly referred to as FB2. This tempered martensitic steel has shown the capacity to withstand temperatures up to 625 °C. FB2 was first created in the European program COST 522, where it showed excellent mechanical properties [12]. This material was mainly investigated on the large scale with forged trail rotors, where both fatigue life and creep properties were investigated [12,13]. However, LCF testing and short-term creep testing are still limited.

FB2 steel has a stable martensitic microstructure with a nominal chemical composition as presented in Table 1. FB2 is a forged steel that has gone through a quality heat treatment of austenitisation at 1100 °C with water spray followed by two stages of tempering at 570 °C and 690 °C respectively [13]. Smooth cylindrical button head specimens, shown in Fig. 1, were manufactured out of FB2 and used for the experimental testing. The gauge section of the specimen has a length of 15 mm and a diameter of 6 mm.

LCF testing was carried out isothermally at different temperatures and total strain ranges, $\Delta\varepsilon_t$. The performed tests include 11 tests without dwell time and 4 tests with 5 min dwell time at both maximum and minimum applied total strain. The experiments were done in strain control with a strain ratio of $R_\varepsilon = -1$ and a strain rate of $\pm\ 10^{-3}$ 1/s. The specimens were cycled until rupture and the failure criteria to determine the number of cycles to failure, N_f, was defined as 25% load drop in the maximum stress. Furthermore, the time to failure, t_f, was also monitored. See Table 2 for details and results from all performed experiments.

The tests with dwell time were designed to introduce stress relaxation behaviour at both tension and compression by holding the total strain constant at both the maximum and minimum load in each cycle. This means that tests with dwell time have spent more time under high temperature in comparison to the ones without dwell (see Table 2).

The machine used for all the experiments was an MTS servo hydraulic rig that was equipped with an MTS 652.01 furnace for high temperature testing. The furnace contains controllable heat units and thermocouples were attached to the specimen to achieve the desired temperature within the gauge section. The total strain was recorded using an Instron 2632–055 extensometer, while the load was obtained from the control unit, Instron 880.

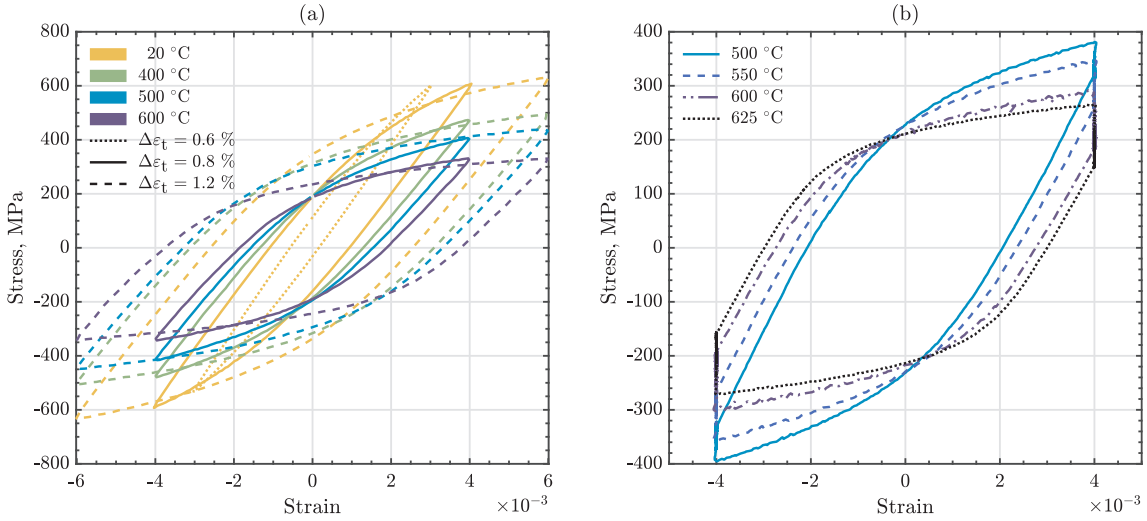

Fig. 3. Mid-life hysteresis loops obtained from experimental LCF tests (a) without dwell time; (b) with 5 min dwell time.

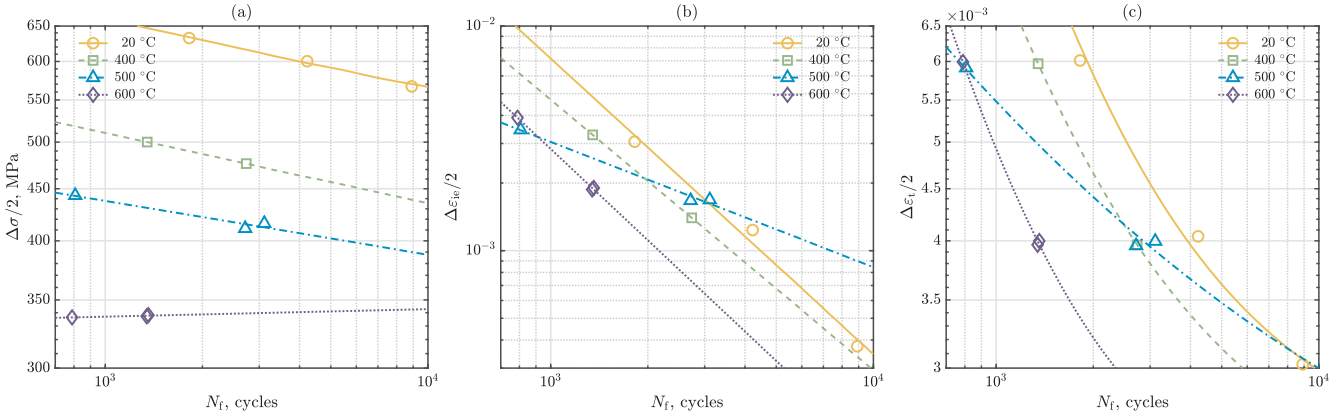

Fig. 4. Fatigue life of LCF tests without dwell time in terms of (a) Stress amplitude, $\Delta\sigma/2$ (Basquin); (b) inelastic strain amplitude, $\Delta\varepsilon_{ie}/2$ (Manson–Coffin); (c) total strain amplitude, $\Delta\varepsilon_t/2$ (Manson–Coffin–Basquin).

Table 3
Fitting parameters for the experimental fatigue life curves.

Temperature, °C	ε_f'	c	σ_f', MPa	b
20	157.33	−1.316	1112.802	−0.06866
400	43.88	−1.202	861.928	−0.06891
500	0.2143	−0.559	653.071	−0.05262
600	84.93	−1.356	318.617	0.00737

Table 5
Temperature dependent material constants, A and n, for the power law creep model.

Temperature, °C	A, 1/(GPa^n·s)	n
500	4.55×10^{13}	43.04
550	1.84×10^{9}	26.80
600	1.54×10^{5}	15.96
625	2.08×10^{3}	12.55

Table 4
Temperature and total strain range dependent material parameters for the elasto-plastic model.

Temperature, °C	$\Delta\varepsilon_t$, %	E, GPa	$\sigma_{y'}$, MPa	C_1, MPa	C_2, MPa	γ_1	γ_2
20	0.6	213.32	300.05	1019030	538798	11996	1491
	0.8	213.32	282.12	534110	197090	4509.3	576.46
	1.2	213.32	308.24	90470	328880	332.96	2687.6
400	0.8	185.92	234.12	125930	488520	502.79	5315.1
	1.2	185.92	218.91	408060	71678	3645.8	352.18
500	0.8	179.28	197.11	91938	331860	430.63	4014.5
	1.2	179.28	195.36	52327	374730	322.62	3179.9
600	0.8	160.27	154.06	82488	504880	562.3	7661.1
	1.2	160.27	151.32	34626	251620	266.26	3054.1

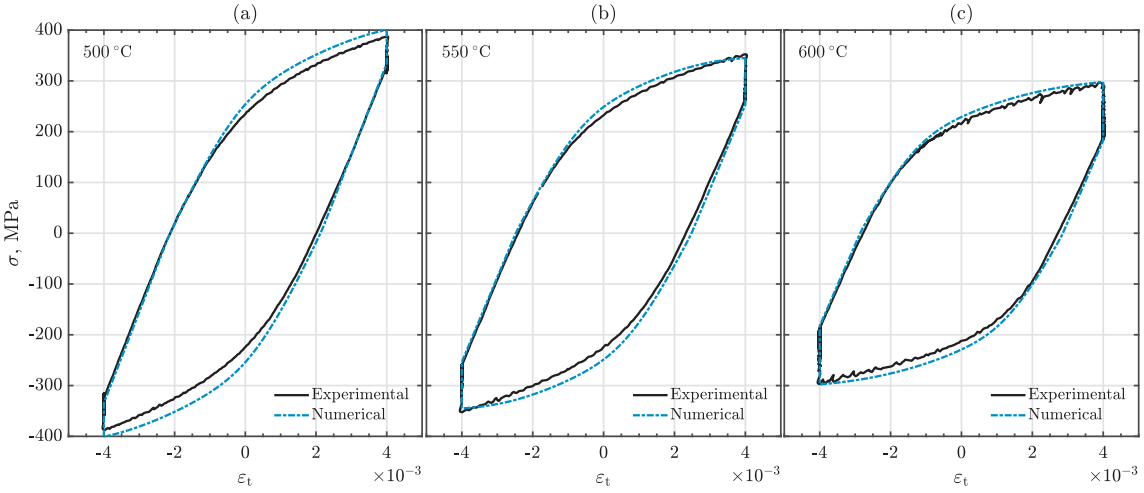

Fig. 5. Experimental and modelled mid-life loops for LCF tests with dwell time at (a) 500 °C; (b) 550 °C and (c) 600 °C.

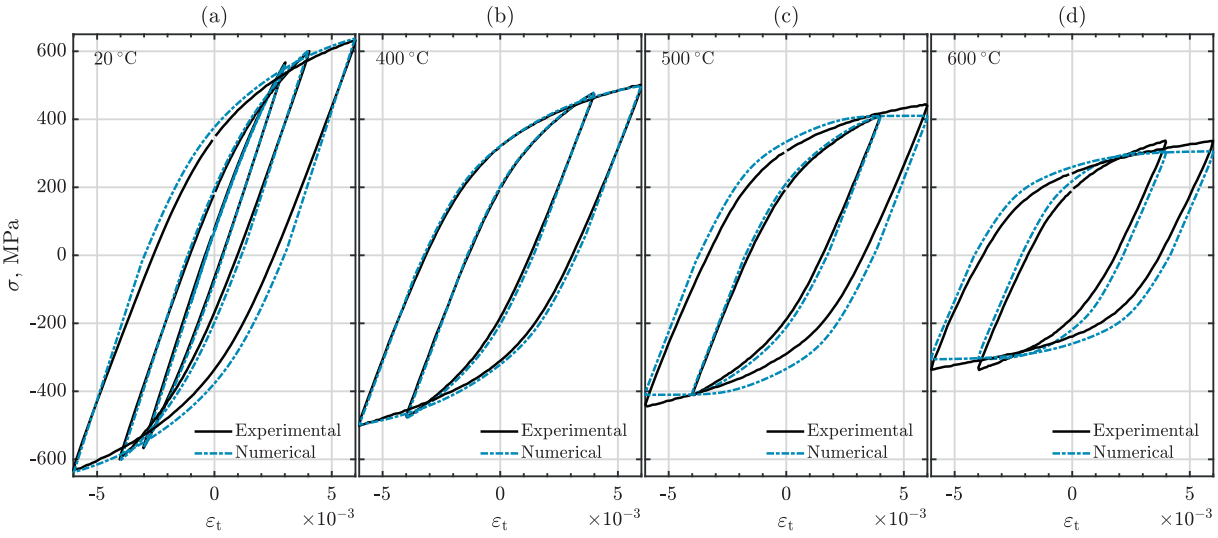

Fig. 6. Experimental and modelled mid-life loops for LCF tests without dwell time at (a) 20 °C; (b) 400 °C; (c) 500 °C and (d) 600 °C.

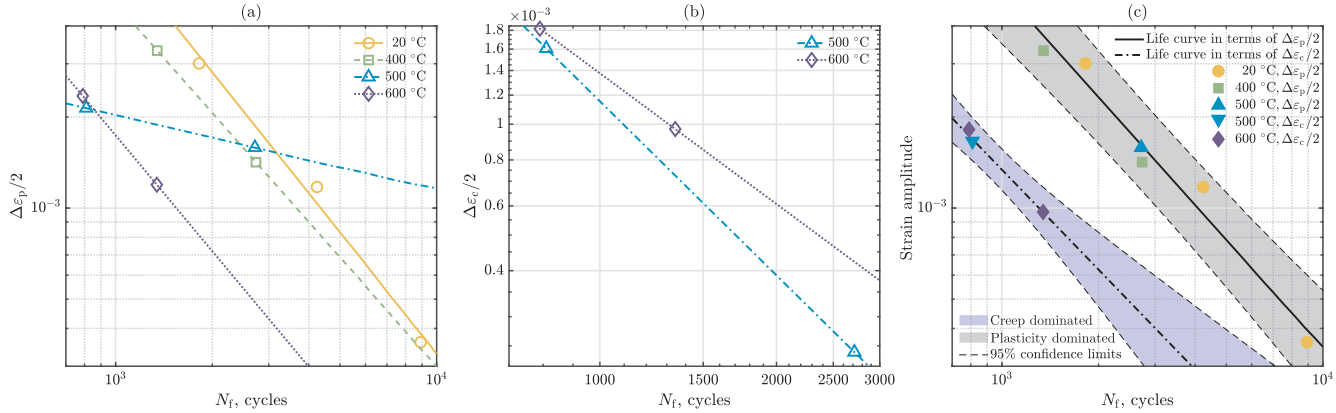

Fig. 7. Modelled fatigue life curves based on (a) plastic strain amplitude, $\Delta\varepsilon_p/2$; (b) creep strain amplitude, $\Delta\varepsilon_c/2$; (c) split regions of plasticity and creep domination (the life curve in solid line is fitted based on $\Delta\varepsilon_p/2$, while the life curve in dashed line is fitted based on $\Delta\varepsilon_c/2$).

3. Microstructural characterisation

The microstructure was inspected using a Hitachi SU-70 field emission gun scanning electron microscope (SEM). This analysis was done on polished samples of the LCF tested specimens after their final rupture. After identifying the initiation zone by fractography the specimen was cut along the stress axis (x-axis) as illustrated in Fig. 2. The sample was then mounted and the cut surface was polished so that the regions directly below and away from the fracture surface are investigated.

The deformed microstructure was qualitatively analysed using the SEM technique electron channelling contrast imaging (ECCI) [14]. A 4-

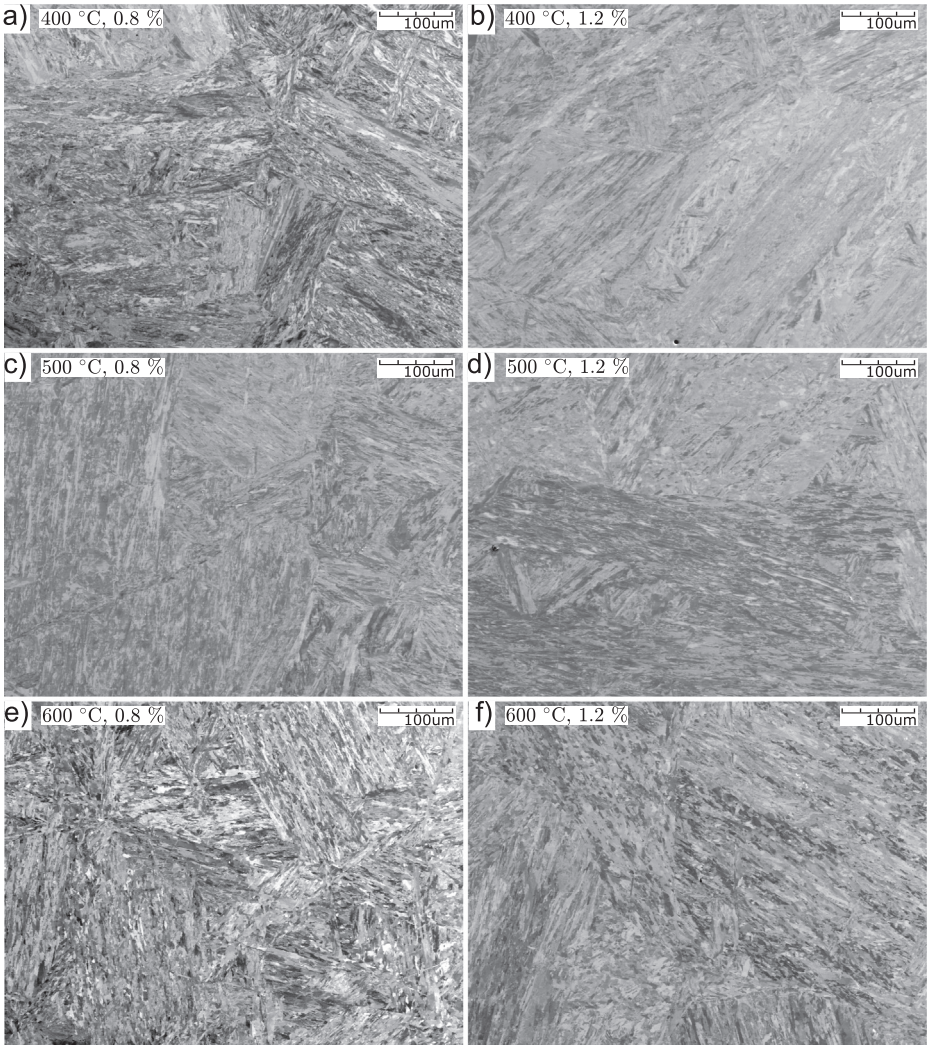

Fig. 8. Backscatter electron micrographs for: (a) 400 °C, $\Delta\varepsilon_t = 0.8\%$; (b) 400 °C, $\Delta\varepsilon_t = 1.2\%$; (c) 500 °C, $\Delta\varepsilon_t = 0.8\%$; (d) 500 °C, $\Delta\varepsilon_t = 1.2\%$; (e) 600 °C, $\Delta\varepsilon_t = 0.8\%$ and (f) 600 °C, $\Delta\varepsilon_t = 1.2\%$.

quadrant solid state backscatter electron detector was used in the ECCI analysis with 7 mm working distance and 10 kV acceleration voltage. To study the crystallographic orientation and measure the plastic deformation, electron backscatter diffraction (EBSD) was employed [15]. The EBSD analysis was performed using 25 mm working distance, 20 kV acceleration voltage, and a step size of 0.2 μm, while the measurements were evaluated using HKL software, Channel 5 [16].

4. Fatigue life evaluation

Cyclic softening was observed for FB2, where the amount of softening depended on both the temperature and the applied total strain range, $\Delta\varepsilon_t$. The fatigue life, N_f, decreased by increasing the temperature and $\Delta\varepsilon_t$ (see Table 2). The LCF tests with dwell time showed a large reduction in N_f compared to the tests without dwell time for the same $\Delta\varepsilon_t$. However, the time to failure, t_f, was much longer. The experimental mid-life hysteresis loops for all performed tests are plotted in Fig. 3. It can be seen that the rise in temperature increases the inelastic strain range, while the stress range drops. An increase in $\Delta\varepsilon_t$ enlarges the stress range for low temperatures but the difference in the stress range disappears by increasing the temperature, especially at 600 °C. The LCF tests with 5 min dwell time showed stress relaxation behaviour at both tension and compression due to the dwell time introduced at both maximum and minimum stress of the cycle. This adds additional damaging mechanisms by causing the stress range to drop even lower than those without dwell time for the same $\Delta\varepsilon_t$. It could be noted that the stress relaxation increases with temperature, e.g. around 63 MPa at 500 °C and around 116 MPa at 625 °C. The stress relaxation during the dwell time was later used to determine the creep properties of the material.

The experimental mid-life hysteresis loop was used to construct the experimental fatigue life model following the Manson–Coffin–Basquin relation in terms of total strain amplitude, $\Delta\varepsilon_t/2$. This relation is basically a combination of the Manson–Coffin equation in terms of the inelastic strain amplitude, $\Delta\varepsilon_{in}/2$, and the Basquin equation in terms of the elastic strain amplitude, $\Delta\varepsilon_e/2$, as

$$\frac{\Delta\varepsilon_t}{2} = \frac{\Delta\varepsilon_e}{2} + \frac{\Delta\varepsilon_{in}}{2}, \qquad \Delta\varepsilon_e = \frac{\Delta\sigma}{E}, \tag{1}$$

where $\Delta\sigma$ and E are the stress range and the elastic modulus, respectively. The Manson–Coffin equation relates the inelastic strain amplitude to the fatigue life, as

$$\frac{\Delta\varepsilon_{in}}{2} = \varepsilon_f'(2N_f)^c \tag{2}$$

where ε_f' and c are temperature dependent material constants [4] referred to as the fatigue ductility coefficient and exponent, respectively. The Basquin equation relates the stress amplitude to the fatigue life, as

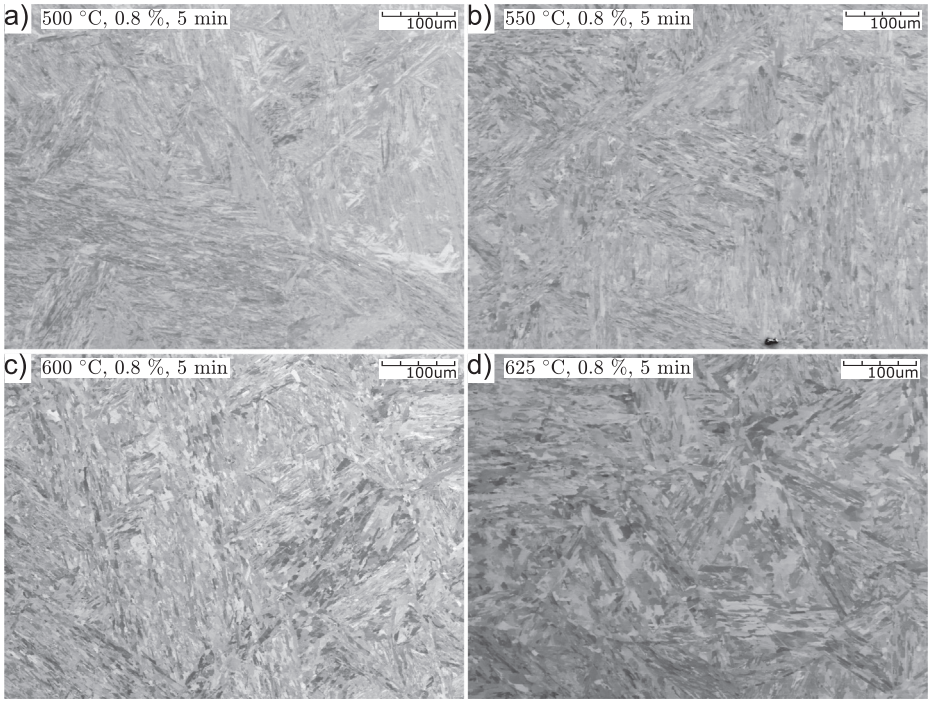

Fig. 9. Backscatter electron micrographs for: (a) 500 °C, $\Delta\varepsilon_t = 0.8\%$, 5 min; (b) 550 °C, $\Delta\varepsilon_t = 0.8\%$, 5 min; (c) 600 °C, $\Delta\varepsilon_t = 0.8\%$, 5 min and (d) 625 °C, $\Delta\varepsilon_t = 0.8\%$, 5 min.

$$\frac{\Delta\sigma}{2} = \sigma_f'(2N_f)^b \tag{3}$$

where σ_f' and b are also temperature dependent material constants [4] called the fatigue strength coefficient and exponent, respectively. The fatigue life relations, taken from the experimental mid-life cycles, are compiled in Fig. 4 as (a) Basquin, in terms of stress amplitude, $\Delta\sigma/2$, (b) Manson–Coffin, in terms of inelastic strain amplitude, $\Delta\varepsilon_{in}/2$, and (c) Manson–Coffin–Basquin, in terms of total strain amplitude, $\Delta\varepsilon_t/2$. The temperature dependent material constants fitted using least squares method are provided in Table 3.

It must be noted that the experimental fatigue life curves at 400 °C were fitted with only two tests done at different $\Delta\varepsilon_t$. However, these fittings were considered acceptable since two repeated tests at 500 °C and 600 °C with $\Delta\varepsilon_t = 0.8\%$ showed small scattering. Moreover, the life curve fitted at 400 °C shows similar behaviour as the one at 20 °C, which was fitted with three different $\Delta\varepsilon_t$ tests. The LCF tests with dwell time were excluded from the fatigue life model due to the additional creep damage introduced during the dwell time compared to a pure cyclic loading. However, the dwell time tests were mainly used to extract the short term creep properties and verify the creep model used.

From the stress-based fatigue life curves, Fig. 4(a), an obvious distinction between the temperatures is provided, but life prediction becomes inapplicable at 600 °C. The stress amplitude, $\Delta\sigma/2$, at 600 °C is nearly constant. This behaviour suggest extensive creep at 600 °C that puts the stress amplitude at almost a constant level for different total strain ranges applied. On the other hand, the strain-based relations, presented in Fig. 4(b) and (c), provide better life prediction. However, the life curve for 500 °C seems to behave differently. The life curve at 500 °C appear to experience two different damage behaviours. At low strain range, the fatigue life at 500 °C approaches that of room temperature and 400 °C, while at high strain range, it approaches that of 600 °C.

The behaviour of the specimen tested at 600 °C and the transition behaviour at 500 °C suggest the existence of two damage mechanisms, plasticity–dominated and creep–dominated, where the transition between these two mechanisms depends both on the temperature and total strain range applied. Thus, in order to construct a more appropriate fatigue life model, the inelastic strain amplitude, $\Delta\varepsilon_{ie}/2$, must be split into plastic strain amplitude, $\Delta\varepsilon_p/2$, and creep strain amplitude, $\Delta\varepsilon_c/2$, following an approach similar to SRP [10]. In this study, an inelastic partitioning approach using FE-analysis has been used.

5. Finite element strain range partitioning

The FE SRP approach presented here aims to split the inelastic strain range of the mid-life cycle of each of the performed test into plastic strain and creep strain. This is done by simulating the experimental mid-life curves using an FE model that includes both cyclic elasto-plastic material model in conjunction with a creep model. Then, the plastic and creep strain amplitudes, obtained from the FE model, are used to define a proper fatigue life model that explains the temperature dependence behaviour of the material.

The elasto-plastic material model used in this study consists of a linear elastic and a nonlinear kinematic hardening law with two back-stresses. This material model is provided by the FE software ABAQUS [17] as a built-in constitutive model. The hardening law for each of the back-stress tensors, $\boldsymbol{\alpha}_k$, is [17]

$$\dot{\boldsymbol{\alpha}}_k = C_k\frac{\boldsymbol{\sigma} - \boldsymbol{\alpha}}{\sigma_{y'}}\dot{\bar{\varepsilon}}^p - \gamma_k\boldsymbol{\alpha}_k\dot{\bar{\varepsilon}}^p \tag{4}$$

with the overall back-stress tensor

$$\boldsymbol{\alpha} = \sum_{k=1}^{2}\boldsymbol{\alpha}_k \tag{5}$$

where $\dot{\boldsymbol{\alpha}}_k$, $\boldsymbol{\sigma}$, $\sigma_{y'}$, and $\dot{\bar{\varepsilon}}^p$ are the time derivative of the back-stress tensor, the stress tensor, cyclic yield strength and the equivalent plastic strain rate, respectively, whereas C_k and γ_k are fitted temperature dependent material parameters with $k = 1$, and 2. The monotonic loading of the first half-cycle for all performed tests was used to obtain the average elastic modulus, E, for each temperature. For the nonlinear kinematic hardening model, the material parameters were fitted to the loading curve of the mid-life cycle for the LCF tests without dwell time (Fig. 3(a)). The fitting parameters extracted from the mid-life cycle are

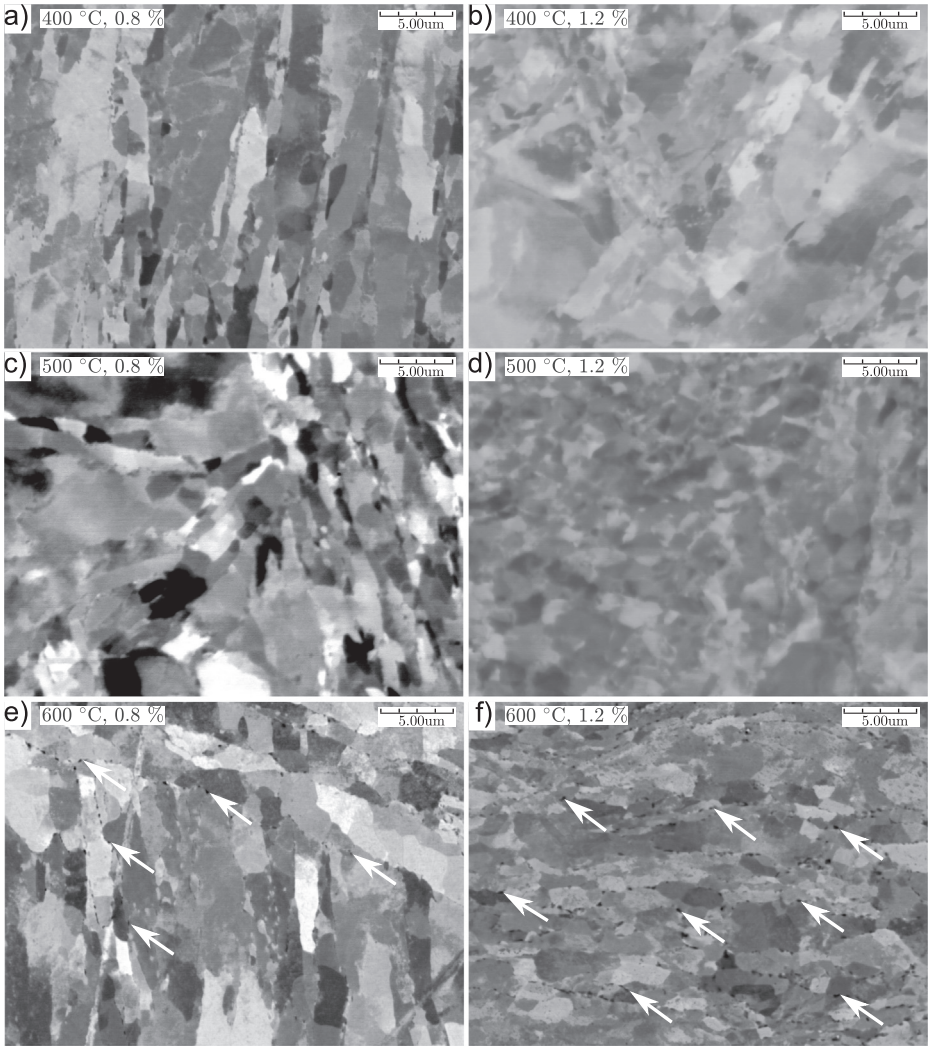

Fig. 10. Backscatter electron micrographs for: (a) 400 °C, $\Delta\varepsilon_t = 0.8\%$; (b) 400 °C, $\Delta\varepsilon_t = 1.2\%$; (c) 500 °C, $\Delta\varepsilon_t = 0.8\%$; (d) 500 °C, $\Delta\varepsilon_t = 1.2\%$; (e) 600 °C, $\Delta\varepsilon_t = 0.8\%$ and (f) 600 °C, $\Delta\varepsilon_t = 1.2\%$. Voids (indicated by white arrow) were visible at grain boundaries for specimens tested at 600 °C, while no voids were observed at 500 °C and below.

dependent on both the temperature and the applied total strain range, $\Delta\varepsilon_t$. The material parameters for the elasto-plastic material model used in this study are presented in Table 4.

The high temperature LCF tests with dwell time were used to calibrate the creep model following a power law [18]

$$\dot{\varepsilon}_{c,d} = A\sigma_d^n \tag{6}$$

where $\dot{\varepsilon}_{c,d}$ and σ_d are the creep strain rate during the dwell time and the stress during the dwell time, respectively. The constants A and n are temperature dependent material fitting parameters. During the dwell time interval, $t_{d,0} \leqslant t \leqslant t_{d,f}$, with t as time, the total strain is held constant while the stress relaxes. By assuming the plastic strain constant while the creep strain, $\varepsilon_{c,d}$, advances equally to the drop in the elastic strain, $\varepsilon_{e,d}$, within the dwell region, the following relation is obtained

$$\dot{\varepsilon}_{c,d} = -\dot{\varepsilon}_{e,d}. \tag{7}$$

where $\dot{\varepsilon}_{e,d}$ is the elastic strain rate during the dwell time. Using $\dot{\varepsilon}_{e,d} = \dot{\sigma}_d/E$ in Eq. (7) then substituting into Eq. (6) and integrating both sides from $t_{d,0}$ to $t_{d,f}$ gives

$$EA\int_{t_{d,0}}^{t} [\sigma_d(t')]^n dt' = \sigma_d(t_{d,0}) - \sigma_d(t), \quad t_{d,0} \leqslant t \leqslant t_{d,f}. \tag{8}$$

The parameters A and n were fitted for a specific dwell region using Eq. (8) by minimising the square of the residual with a simplex search method, fminsearch, in Matlab [19]. A trapezoid quadrature was used to estimate the integration. To calibrate the temperature dependent creep model, the fitting parameters A and n were found for all cycles of the LCF tests with dwell. Due to the isotropic behaviour of the creep in tension and compression, the fitting parameters were only taken from the dwell time region in tension. Furthermore, an average value of the creep parameters within 20–80% of the fatigue life were taken for each test. The parameter A was then fitted using an Arrhenius type of equation while n was fitted with a 2nd order polynomial. To accommodate a better creep model fit, the creep parameters at 500 °C were taken from a cycle with less creep, as the first approach generated an unnecessary high creep strain. Table 5 shows the fitted creep parameters.

To carry out the simulations with simultaneous plasticity and creep, an FE model was built using ABAQUS, which included both the elasto-plastic and the creep models discussed earlier. The constructed FE model used a simplified geometry, which is a unit cube with a uniform mesh of 8 quadratic hexahedral elements (20-node brick elements) with reduced integration. The model has been constrained to prevent rigid body motions, where a surface on the cube was fixed in the normal direction and two corner nodes on the same edge of that surface were constrained to prevent translation and rotation. A prescribed displacement set on a surface, opposite to the constrained one, was used to simulate the total strain applied on the body.

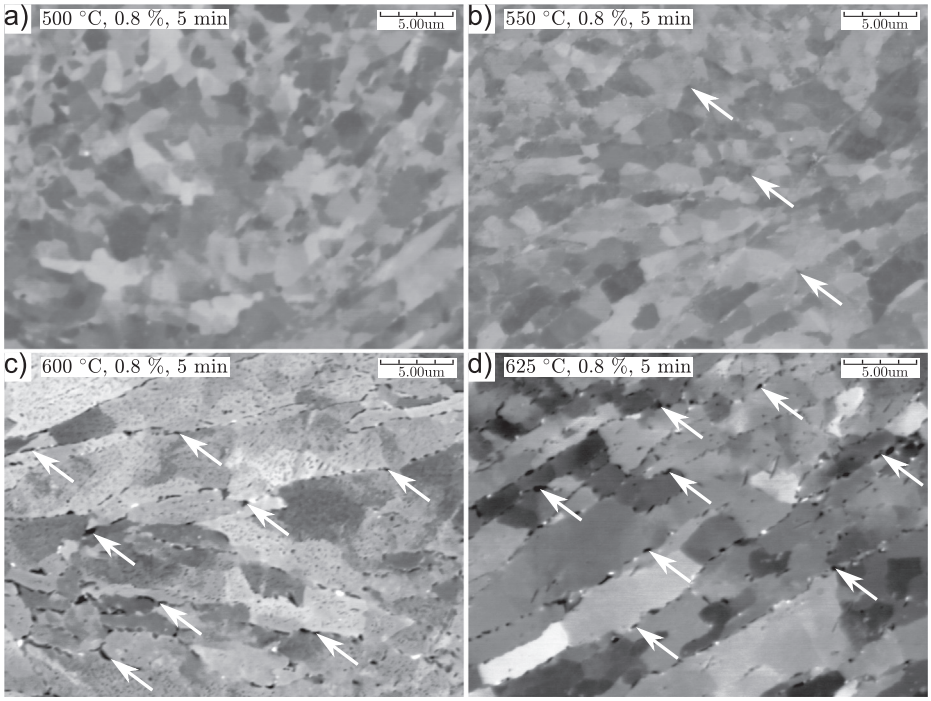

Fig. 11. Backscatter electron micrographs for: (a) 500 °C, $\Delta\varepsilon_t = 0.8\%$, 5 min; (b) 550 °C, $\Delta\varepsilon_t = 0.8\%$, 5 min; (c) 600 °C, $\Delta\varepsilon_t = 0.8\%$, 5 min and (d) 625 °C, $\Delta\varepsilon_t = 0.8\%$, 5 min. Voids (indicated by white arrows) were visible at grain boundaries for specimens tested at 625 °C and 600 °C, while few voids were observed at 550 °C and no voids seen at 500 °C.

The calibrated creep model was verified by modelling the experimental mid-life hysteresis loops with 5 min dwell time (Fig. 3(b)). The temperature dependent material parameters, used for the elasto-plastic model to simulate these LCF tests with dwell time, were taken from the largest total strain range, i.e. $\Delta\varepsilon_t = 1.2\%$. Fig. 5 shows the modelled and experimental hysteresis loops for tests at 500 °C, 550 °C and 625 °C. As seen, the agreement between experimental and modelled hysteresis loops is acceptable and the stress relaxation behaviour between them seems to agree.

The experimental mid-life hysteresis loops without dwell time (Fig. 3(a)) were then modelled using the temperature and total strain range dependent elasto-plastic parameters along with the temperature dependent creep parameters. The experimental and modelled mid-life hysteresis loops for all LCF tests without dwell are presented in Fig. 6. The combined plasticity and creep models implemented in the modelled mid-life curves seem to predict the actual data fairly well. By using the built-in routines in ABAQUS, plasticity and creep were uncoupled. This approach is considered usable since the numerical results reproduce the experimental hysteresis curves with acceptable accuracy (see Figs. 5 and 6).

Since the modelled loops include combined plasticity and creep, the FE model allows to split the inelastic strain of each cycle into plastic strain and creep. The obtained plastic strain amplitude, $\Delta\varepsilon_p/2$, and creep strain amplitude, $\Delta\varepsilon_c/2$, are plotted versus the fatigue life in Fig. 7(a) and (b), respectively, for all LCF tests without dwell. The lines were fitted using the Manson–Coffin type of equation (Eq. (2)). The model predicts large creep at 600 °C, while close to no creep at 400 °C and below for all total strain ranges applied. However, at 500 °C creep seems to depend on the total strain range used. At low total strain range ($\Delta\varepsilon_t = 0.8\%$), the specimen tested at 500 °C experienced very low amount of creep while, at high total strain range ($\Delta\varepsilon_t = 1.2\%$), the amount of creep was high. The proposed model suggests the existence of two fatigue damage mechanisms and the transition between them occur at 500 °C depending on the strain range level applied. Thus, taking into account the existence of two regions (creep and plasticity dominated), two fatigue life curves could be constructed, one in terms of $\Delta\varepsilon_p/2$ that includes all tests with low creep strain, and the other in terms of $\Delta\varepsilon_c/2$ that includes all tests with large creep strain, as shown in Fig. 7(c). Two regions could be established, plasticity-dominated and creep-dominated, that were determined using the 95% confidence limits. This split into two regions also seems to largely explain the temperature dependence of the fatigue life, i.e. at high temperature the life is largely affected by creep becoming active.

6. Microstructure analysis

Fig. 8 shows the backscatter electron micrographs for all LCF tests without dwell time except the tests done at room temperature, while Fig. 9 shows all the LCF tests with dwell. These micrographs were taken from a position far from the fracture surface and with low magnification. In general, no significant difference was observed in the microstructure other than the martensitic laths coarsening with increase in temperature which becomes more visible for the tests with dwell time, see Fig. 9.

At higher magnification, some specimens showed distinctive features at the grain boundaries that are likely voids. These voids, when present, were limited within a region close to the fracture surface. This indicates that thermal exposure alone was not the main trigger for these features, since no voids were visible away from the fracture surface. Thus, these features were not mistaken as to be precipitates. For all the tests performed at 400 °C and 500 °C, no voids were identified, see Fig. 10(a)–(d) and Fig. 11(a). However, at higher temperature, 550 °C and above, voids were found at the grain boundaries with different level of visibility depending on the temperature and dwell time used. At 600 °C, the specimen tested at $\Delta\varepsilon_t = 1.2\%$ showed more voids with larger sizes compared to the one tested at $\Delta\varepsilon_t = 0.8\%$, as seen in Fig. 10(e) and (f). The voids seem to decrease in number and size for the sample tested at 550 °C with dwell, see Fig. 11(b). The dwell time tests done at 600 °C and 625 °C showed the highest number and largest grain boundary cavitations, which suggests the coalescence of voids, see Fig. 11(c) and (d). Voids in the grain boundaries close to the fracture surface are believed to occur due to creep-fatigue interaction [20,21].

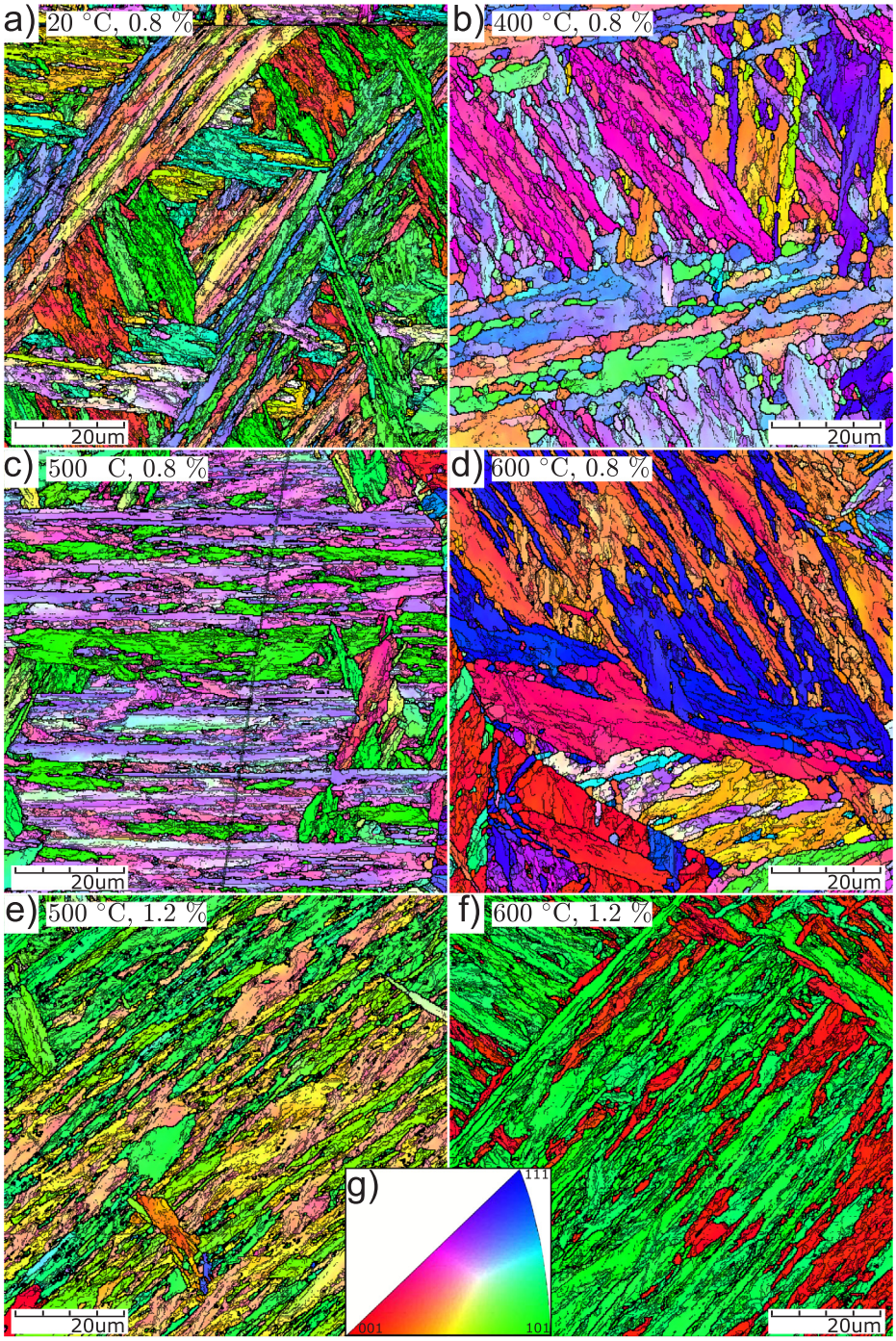

Fig. 12. Grain structures and LAGBs (black lines) shown by EBSD maps for specimens tested at: (a) 20 °C, $\Delta\varepsilon_t$ = 0.8%; (b) 400 °C, $\Delta\varepsilon_t$ = 0.8%; (c) 500 °C, $\Delta\varepsilon_t$ = 0.8%; (d) 600 °C, $\Delta\varepsilon_t$ = 0.8%; (e) 500 °C, $\Delta\varepsilon_t$ = 1.2% and (f) 600 °C, $\Delta\varepsilon_t$ = 1.2%. The color map is based on inverse pole figure, (g).

Thus, the existence of voids indicate that a significant portion of the inelastic strain comes from creep deformation, besides the plastic deformation.

The fatigue life model, that describes the split between plasticity dominated and creep dominated regions, is supported by the existence of voids at 600 °C and the lack of voids at 400 °C. The fatigue model predicts that the transition between these two regions must occur at 500 °C, where creep is sensitive to the strain range applied. However, the micrographs show no voids in any of the 500 °C tests without dwell. Thus, determining this transition region would not be obvious from only observing the existence of voids. Furthermore, dwell time test at 500 °C did not show any clear existence of voids, although stress relaxation still occurred. This indicates that other creep mechanisms, such as diffusion flow or dislocation climbing, could occur before grain boundary sliding. These mechanisms should, however, affect the fraction of low angle grain boundaries (LAGBs) detected in the EBSD.

The plastic deformation could be quantified using EBSD by measuring the fraction of LAGBs [15]. EBSD maps of the polished LCF samples taken away from the fracture surface were used to visualise the crystallographic misorientations, which are the difference in the orientation between two measured points next to each other, see Fig. 12. The black lines within the EBSD maps represent the LAGBs, which are the misorientation between 1° and 10°, while the white lines represent high angle grain boundaries which has a misorientation larger than 10°.

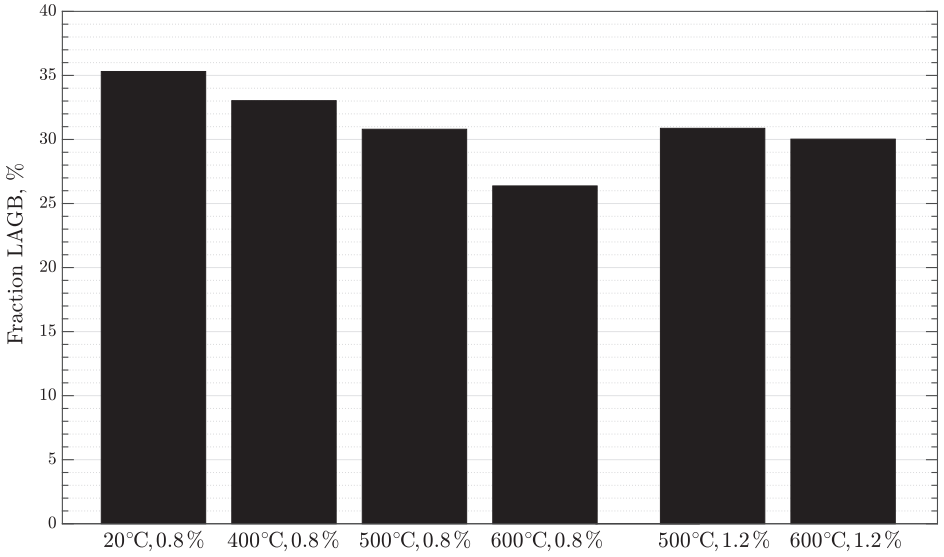

Fig. 13. LAGBs fraction for 6 tested specimens without dwell time.

The amount of LAGBs quantified from the EBSD results, as percentage fraction, are shown in Fig. 13. The fraction of LAGBs seems to differ among the observed samples except for the specimens tested at 500 °C. The highest amount of LAGBs fraction was seen for the specimen tested at 20 °C with $\Delta\varepsilon_t = 0.8\%$. The increase in temperature seems to reduce the fraction of LAGBs for both $\Delta\varepsilon_t$. Interestingly, the increase in $\Delta\varepsilon_t$ seems to increase the LAGB for only the samples tested at 600 °C.

Comparing the fraction of LAGBs from Fig. 13 with the inelastic strain amplitude from the experimental mid-life curves (Fig. 4(b)), a discrepancy can be noticed. The increase in temperature increases the amount of inelastic strain range while it reduces the fraction of LAGBs for both $\Delta\varepsilon_t = 0.8\%$ and $\Delta\varepsilon_t = 1.2\%$. Since low angle grain boundaries are associated with plastic deformation [15], the lower fraction of LAGBs at 600 °C, $\Delta\varepsilon_t = 0.8\%$, suggests that a substantial part of the inelastic strain is creep strain. Conversely, the specimen with the lowest inelastic strain range (tested at 20 °C, $\Delta\varepsilon_t = 0.8\%$) had the highest fraction of LAGBs, and thus experienced more plasticity. Furthermore, the increase in $\Delta\varepsilon_t$ at 500 °C increased the inelastic strain amplitude, while the amount of LAGB observed was the same. This indicates that samples tested at 500 °C experiences the same amount of plastic deformation (as their fraction of LAGBs is similar) even though the applied total strain range is different. Thus, the increase in the inelastic strain amplitude displayed at 500 °C, $\Delta\varepsilon_t = 1.2\%$ is attributed to another type of deformation, i.e. creep. It could be argued that a lower fraction of LAGBs at higher temperatures is also due to annihilation of dislocations through recrystallisation. However, no significant recrystallisation was observed. Again, the above results indicate that large deformation at high temperatures results in significant amounts of creep strain rather than extensive plastic strain.

7. Conclusion

The steam turbine rotor steel FB2 was tested in LCF, both with and without dwell time. The material behaviour at mid-life was modelled and the LCF tests with dwell time were used to extract creep properties. Fatigue life models based on stress and strain from the experimental mid-life cycles were presented and seemed to work excellently for low temperatures (400 °C and below). At high temperatures, complications were introduced to the fatigue life analysis, which is mainly influenced by significant amounts of creep. Neither the stress amplitude, the inelastic strain amplitude, nor the total strain amplitude can be used as a predictive tool for LCF within the strain and temperature ranges relevant to steam turbine rotor materials operating at ultra-supercritial steam conditions.

A partition of the inelastic strain amplitude into plastic and creep components is possible through FE analysis. By separately considering the effects of plastic strain amplitude and creep strain amplitude on the number of cycles to failure, two regimes of fatigue damage could be identified and the transition between these depends on both temperature and total strain range applied. A plasticity-dominated regime was observed for 400 °C and below, and for low total strain range at 500 °C. Outside these conditions, creep dominates the fatigue life. It is anticipated that the creep properties are pivotal to the fatigue life of FB2 in the high-temperature conditions of ultra-supercritial steam turbine rotor applications.

Microstructural investigation (including EBSD mapping) of ruptured specimens revealed that grain boundary voids were detected in specimens tested at 600 °C, indicating significant creep at this temperature. Voids did not only occur for the dwell time test but also for the pure cyclic cases, indicating rapid creep rate at this temperature (i.e. 600 °C). The fraction of low angle grain boundaries (which can be taken as an indication of plastic deformation) was seen to decrease with the increase in the inelastic strain range and temperature for all applied total strain ranges. It is considered likely that a significant amount of the inelastic strain at high temperatures is creep strain, which may lead to a different damage mechanism compared to specimens tested at lower temperatures.

Declaration of Competing Interest

The authors declare that they have no known competing financial interests or personal relationships that could have appeared to influence the work reported in this paper.

Acknowledgment

This project has received funding from the European Union's Horizon 2020 research and innovation programme under grant agreement No. 764545.

References

[1] S. Holdsworth, Creep-resistant Materials for Steam Turbines, May 2015, Elsevier Ltd., 2004, https://doi.org/10.1016/b0-08-043152-6/00334-x.
[2] A.D. Gianfrancesco, Materials for Ultra-Supercritical and Advanced Ultra-Supercritical Power Plants, Elsevier, 2017.
[3] L. Yimin, W. Jinrui, Low-cycle fatigue behaviour of 30Cr2MoV steel at elevated

temperatures, Int. J. Fatigue 14 (1992) 169–172.
[4] R. Mishnev, N. Dudova, R. Kaibyshev, Low cycle fatigue behavior of a 10Cr–2W–Mo–3Co–NbV steel, Int. J. Fatigue 83 (2015) 344–355.
[5] K. Guguloth, S. Sivaprasad, D. Chakrabarti, S. Tarafder, Low-cyclic fatigue behavior of modified 9Cr-1Mo steel at elevated temperature, Mater. Sci. Eng., A 604 (2014) 196–206.
[6] S.S. Manson, G.R. Halford, Fatigue and durability of structural materials, ASM International, Materials Park, Ohio 44073–0002, 2007.
[7] E. Vacchieri, Review: Creep-fatigue Interaction Testing and Damage Assessment for High Temperature Materials, Elsevier Ltd., 2016.
[8] B. Fournier, M. Salvi, F. Dalle, Y. De Carlan, C. Caës, M. Sauzay, A. Pineau, Lifetime prediction of 9–12%Cr martensitic steels subjected to creep-fatigue at high temperature, Int. J. Fatigue 32 (2010) 971–978.
[9] C. Cristalli, P. Agostini, D. Bernardi, N. Bettocchi, L. Masotti, S. Storai, Low cycle fatigue, creep-fatigue and relaxation-fatigue tests on P91, J. Phys. Sci. Appl. 7 (2017) 18–26.
[10] S.S. Manson, G.R. Halford, M.H. Hirschberg, Creep–fatigue analysis by strain-range partitioning, NASA Technical Memorandum TMX-67838, Lewis Research Center, Cleveland, Ohio, 1971.
[11] R. Mishnev, N. Dudova, R. Kaibyshev, Effect of the strain rate on the low cycle fatigue behavior of a 10Cr-2W-Mo-3Co-NbV steel at 650 °C, Int. J. Fatigue 100 (2017) 113–125.
[12] T.-U. Kern, M. Staubli, B. Scarlin, The European efforts in material development for 650 °C USC Power plants. COST522, ISIJ Int. 42 (2008) 1515–1519.
[13] A. Di Gianfrancesco, L. Cipolla, D. Venditti, S. Neri, M. Calderini, Creep behaviour and microstructural analysis of fb2 trial rotor steel, 2008, pp. 366–376. https://doi.org/10.1361/cp2007epri0366.
[14] I. Gutierrez-Urrutia, S. Zaefferer, D. Raabe, Electron channeling contrast imaging of twins and dislocations in twinning-induced plasticity steels under controlled diffraction conditions in a scanning electron microscope, Scripta Mater. 61 (2009) 737–740.
[15] M. Lundberg, J. Saarimäki, J. Moverare, M. Calmunger, Surface integrity and fatigue behaviour of electric discharged machined and milled austenitic stainless steel, Mater. Charact. 124 (2017) 215–222.
[16] Channel 5, Oxford Instruments HKL, 2007.
[17] ABAQUS User's Manual, Version 2017, Dassault Systemes, Johnston, RI, USA, 2017.
[18] W.F. Hosford, Mechanical Behavior of Materials, 2nd ed., Cambridge University Press, 2009, https://doi.org/10.1017/CBO9780511810923.
[19] MathWorks, MATLAB Documentation (R2019a), 2019.
[20] R. Hales, A quantitative metallographic assessment of structural degradation of type 316 stainless steel during creep-fatigue, Fatigue Fracture Eng. Mater. Struct. 3 (1980) 339–356.
[21] W. Zhang, X. Wang, H. Chen, T. Zhang, J. Gong, Microstructural damage mechanics-based model for creep fracture of 9%cr steel under prior fatigue loading, Theoret. Appl. Fract. Mech. 103 (2019) 102269.